



Title	Aseismic strike-slip associated with the 2007 dike intrusion episode in Tanzania
Author(s)	Himematsu, Yuji; Furuya, masato
Citation	Tectonophysics, 656, 52-60 https://doi.org/10.1016/j.tecto.2015.06.005
Issue Date	2015-06-14
Doc URL	http://hdl.handle.net/2115/66170
Rights	©2015, Elsevier. This manuscript version is made available under the CC-BY-NC-ND 4.0 license http://creativecommons.org/licenses/by-nc-nd/4.0/
Rights(URL)	http://creativecommons.org/licenses/by-nc-nd/4.0/
Type	article (author version)
File Information	Manuscript_rev2_finalver2[TECTO10153R2].pdf



[Instructions for use](#)

20 *Abstract*

21 In July 2007, an earthquake swarm initiated in northern Tanzania near Lake Natron
22 and lasted for about two months. Mt. Oldoinyo Lengai, located to the southwest of the
23 swarm, began to erupt effusively about a month prior to the swarm, and increased its
24 eruption intensity on September when the swarm almost ceased. Several previous
25 studies have already reported the crustal deformation signals associated with the swarm
26 using Interferometric Synthetic Aperture Radar (InSAR). However, nearly all the
27 published data are based on the C-band ENVISAT/ASAR images acquired only from
28 the descending path. We use the L-band ALOS/PALSAR images acquired from both
29 ascending and descending paths, which allow us to examine the deformation signals in
30 more detail. In addition to the InSAR data, we employ the offset-tracking technique to
31 detect the signals along the azimuth direction. Using InSAR and offset-tracking data, we
32 obtain the full 3D displacement fields associated with the episode. Besides the
33 horizontal extension and subsidence signals due to the dike intrusion as already reported,
34 the inferred full 3D displacements further indicate that the subsiding zone was
35 horizontally moving by ~48 cm toward SSW. To explain the displacements, we
36 performed fault source modeling, assuming an elastic half space. The fault slip
37 distribution indicates that the contribution of the strike slip component is about 20 % of

38 total moment release. Because almost all the focal mechanisms of earthquakes during
39 the 2007 event indicate nearly pure normal faulting, aseismic strike-slip must have been
40 responsible for the horizontal movement of the subsiding zone. The strike-slip at the
41 shallowest depths suggests the presence of transtensive stress, which seems to be
42 reasonable to generate the relay zones that are widely observed in the East African Rift.
43 We also confirmed that the stress changes due to the dike intrusion were consistent with
44 the inferred fault slip distributions.

45

46 ***Keyword***

47 East African Rift valley; InSAR; Aseismic slip; Transfer zone; Relay ramp; Dike
48 intrusion;

49

50

51 ***1. Introduction***

52 The East African Rift valley (EAR) is a divergent plate boundary between Nubian
53 plate and Somalian plate that extends the length of ~5000 km-long from Ethiopia to
54 Mozambique (e.g., McKenzie et al., 1970; Ebinger, 1989). The EAR contains numerous
55 normal faults and Quaternary active volcanoes along the rift (e.g., Hamling et al., 2009;

56 Paquet et al., 2007). Also, moderate-sized earthquakes frequently occur along the plate
57 boundary (e.g., Chorowicz, 2005).

58 Northern Tanzania is located in the middle of the EAR, and the relative opening rate is
59 2-4 mm/yr along the E-W direction according to the GPS measurement (Stamps et al.,
60 2008; Saria et al., 2014).

61 The 2007 swarm near the Lake Natron started on July 12 (e.g., Calais et al., 2008). The
62 largest earthquake with moment magnitude (M_w) 5.9 occurred on July 17, and the
63 swarm activity continued until the middle of September 2007 (Fig. 1). The
64 campaign-based local seismic network revealed the details of spatial-temporal
65 distribution of epicenters, indicating a migration of earthquake swarm from a deeper
66 depth to the SW toward a shallower depth in the NE (Albaric et al., 2010). Albaric et al.
67 (2010) and Global CMT catalogue (<http://www.globalcmt.org>) reported that eight
68 earthquakes with magnitude larger than 5 occurred during the event, all of which
69 indicated ENE-WSW striking normal fault at depths shallower than 20 km. A swarm of
70 more 1400 earthquakes was recorded for 180 days by a campaign seismic network since
71 June 1 (Albaric et al., 2010).

72 Earthquake swarms are often accompanied with magma intrusion (e.g., Aoki et al.,
73 1999). Mt. Oldoinyo Lengai located about 20 km to the SW from the swarm, is one of

74 the most active volcanoes along the EAR. In 2007, an effusive eruption started one
75 month prior to the swarm activity for the first time in 24 years. The eruptive activity of
76 Mt. Oldoinyo Lengai abruptly switched to episodic explosive eruptions when the swarm
77 activity was decaying in September and continued until April 2008.

78 Several previous studies have already reported the crustal deformation signals
79 associated with the swarm by using satellite synthetic aperture radar (SAR) data (Baer
80 et al., 2008; Calais et al., 2008; Biggs et al., 2009). Calais et al. (2008) pointed out the
81 presence of aseismic slow slip besides the dike intrusion, and examined the details of
82 the dike intrusion processes using the high temporal resolution SAR data. Baer et al.
83 (2008) examined the Coulomb stress changes associated with the event to study the
84 interaction of each fault source. Biggs et al. (2009) studied the relationship between the
85 length of dike and the size of magma chamber compared with those in Afar and Iceland
86 events. In regards to the relationship between the Oldoinyo Lengai eruption and the
87 swarm, Baer et al. (2008) considered that the passage of the seismic-wave through the
88 magma chamber could dynamically trigger the eruption, whereas Biggs et al. (2009)
89 reported that there was no relationship between the eruption and the swarm due to the
90 ground deformation spanning 2001-2004 implies no significant pressure changes in
91 magma chamber. Thus, the interrelation between the eruption and the event is still

92 uncertain.

93 The objectives of this paper are to report the three-dimensional (3D) displacement
94 fields that have never been reported by the previous studies and to show our source
95 modeling results. This was made possible by a couple of reasons. Firstly, in contrast to
96 the previous studies, we used L-band ALOS/PALSAR images acquired from both
97 ascending and descending tracks. The L-band SAR is more advantageous in terms of the
98 easiness of phase unwrapping even the areas with large phase gradient. Secondly, we
99 apply both InSAR and offset-tracking methods that can reveal the full 3D displacements.
100 Based on the inferred fault slip model, we also discuss the implications for the regional
101 stress field and their possible role for the generation of fault segmentation along the rift
102 axes. Moreover, we point out the possibility of the aseismic slip as the driver of
103 earthquake swarm.

104

105 **2. Data processing and SAR observation**

106 Satellite-based SAR is helpful to obtain ground surface deformation signals with
107 unprecedented spatial resolution over wide areas (e.g., Massonnet and Feigl, 1998;
108 Hanssen et al., 2001). We detected the deformation signals associated with the 2007
109 event using both ascending and descending ALOS/PALSAR (L-band, 23.6 cm wave

110 length) images (Table 1), providing us with the range changes along the radar line of
111 sight (LOS) from two independent directions.

112 We also applied the offset-tracking method to derive the displacements projected
113 along the satellite flight direction. We could thus derive the 3D displacements associated
114 with the entire episode. The off-nadir angles are 34.3° for both tracks. The ascending
115 data set (7 July 2007 to 7 October 2007) and the descending data set (5 June 2007 to 13
116 June 2010) cover the entire swarm period (Fig. 1). While the temporal coverage of the
117 descending InSAR image is much longer than that of the ascending InSAR image,
118 because no descending images were acquired between July 2007 and June 2010, and the
119 descending InSAR could include post-seismic deformation signals. However we
120 confirmed insignificant deformation signals after October 2007 from the ascending
121 post-seismic interferogram (7 October 2007 to 15 July 2010) that revealed very little
122 deformation (Fig. S2). To remove the topographic fringes in InSAR data, we used the 3
123 arc-second (90 m) Shuttle Radar Topography Mission (SRTM) digital elevation model
124 (DEM) (Farr et al., 2007). SAR data were processed by GAMMA software (Wegmüller
125 and Werner, 1997). Although we corrected for the orbital and topographic fringes with
126 the use of precision orbit data by JAXA and SRTM DEM, respectively, there still
127 remain long-wavelength phase trends and topography-correlated fringes. The effects of

128 long-wavelength trend and topographic-correlated atmospheric delay in the
129 interferograms were removed, by fitting low-order polynomials and DEM, respectively.
130 For phase unwrapping, we used the branch-cut algorithm (Goldstein et al., 1988). While
131 the unwrapping error would appear at different locations in the ascending and
132 descending data, we confirmed that the phase discontinuities were observed at the same
133 locations, suggesting that they are real deformation signals.

134 The observed InSAR data for both ascending and descending tracks are shown in Figs.
135 2a and 2d. They are resampled with the quad-tree algorithm to effectively reduce the
136 number of data points from ~25000 to ~4000 (Jónnson et al., 2002). The two
137 interferograms indicate two clear phase discontinuities around the center of the graben
138 that strike NE-SW (36.10E, 2.66S – 36.01E, 2.77S) and NNW-SSE (36.05E, 2.63S –
139 36.05E, 2.71S). We also identify another phase discontinuity to the NE that is
140 particularly clear in Fig. 2a. The area between the two discontinuities indicates an
141 increase in the radar line of sight (LOS) in both ascending (Fig 2a) and descending data
142 (Fig. 2d), suggesting that the area has subsided. In contrast, outside this region the
143 signal in the ascending and descending data is opposite, suggesting E-W motion (Figs.
144 2a and 2d). We can thus roughly interpret that the LOS-increasing area was subsiding,
145 and that the outer eastern and western areas were moving to the east and west,

146 respectively. The interferograms indicate that the subsidence area covers 3-4 km width
147 and 13-15 km length. The maximum positive range changes are 46 and 63 cm in
148 ascending and descending data, respectively. Overall, the spatial pattern of the
149 deformation signals looks like a graben structure, which has been reported at other
150 rifting episodes such as the 2009 western Arabia, the 2007 Dallol, and the 1998 Réunion
151 island (Bear and Hamiel, 2010; Nobile et al., 2012; Fukushima et al., 2010). As shown
152 below, however, the azimuth offset data exhibit some unexpected signals.

153 Azimuth offset data derived from the ascending path similarly indicates two
154 discontinuities (Fig. 3a) that are compatible with the expanding areas with E-W motion
155 in the interferograms (Figs. 2a and 2d). The most remarkable point is that the subsiding
156 zone indicates ~40 cm negative offset, which indicates that the area has moved opposite
157 to the satellite flight direction. Namely, the central subsiding region was not only
158 subsiding but also moving horizontally, because the azimuth offsets have no sensitivities
159 to the vertical displacements. Although the azimuth offset derived from the descending
160 pair is much noisier due to the lower-coherence, the data set also exhibits small
161 horizontal displacements that are nearly in parallel with the satellite flight direction (Fig.
162 S1). The azimuth offset data from both ascending and descending tracks thus
163 unambiguously indicate horizontal displacements of a subsiding graben structure. Biggs

164 et al. (2009) showed a result from multiple aperture InSAR (MAI) measurement
165 (Bechor and Zebker 2006), which are quite consistent with Fig 3a in terms of both the
166 signal amplitude and the deforming area. Nevertheless, they dismissed the MAI
167 observation in their analyses, probably because there were no other independent data
168 that could support the signal.

169 We calculated 3D displacements from the ascending and descending interferograms
170 and the azimuth offset (Fig. 5a) (Fialko et al., 2001). The orange lines in Fig. 4 show the
171 locations for the top edges of our fault source models shown below. The interval of the
172 observation point is 2×2 km. The lack of the points around the summit of Mt. Gelai is
173 because the azimuth offsets are noisier than InSAR data and thus such area are masked.

174 The horizontal displacements in Fig. 5a indicate that the western and the eastern half of
175 the areas moved up to ~35 cm toward W-WSW and ~51 cm toward E-NE, respectively.

176 The subsidence zone moved toward SSW direction with a maximum horizontal
177 displacement of ~48 cm. The vertical displacements are shown in Fig. 5b, which
178 indicates that the eastern half was uplifting and the center area was subsiding by ~62 cm.

179 In contrast, the western half was uplifting by only a few centimeters.

180

181

182 **3. The elastic dislocation source modeling**

183 Static ground displacements associated with earthquakes and/or dike intrusion
184 episodes are often interpreted by using analytical solutions due to planar rectangular
185 dislocation elements in elastic half-space (Okada, 1985). In this study, we estimate
186 non-planar fault planes based on the analytical solutions due to triangular dislocation
187 elements because the observations reveal complex deformation signals. The triangular
188 dislocation elements are advantageous because it can represent non-planar fault planes
189 without making unrealistic overlaps or gaps (Maerten et al., 2005; Furuya and Yasuda,
190 2011). To calculate the ground deformation due to the triangular dislocation elements,
191 we use the MATLAB script that is made available by Meade (2007). To generate the
192 mesh coordinates for the non-planar planes, we used Gmsh software (Geuzaine and
193 Remacle, 2009).

194 Almost all the focal mechanisms of the earthquakes during the event show normal
195 faulting. We set a west-dipping and an east-dipping fault whose top edges can match the
196 locations off the phase discontinuities in the interferograms (Fig.4, 6); the other
197 parameters for the fault geometry, the bottom location and depth, were estimated by
198 trial-and-errors (e.g., Furuya and Yasuda, 2011). We set another west-dipping fault at the
199 eastern flank of Mt. Gelai (Figs. 6e-f), because the two interferograms indicate a phase

200 discontinuity at the same location. The deformation pattern is consistent with a dike
201 intrusion and can be modeled as a tensile opening dislocation source. We set a vertical
202 tensile dislocation source as the dike segment, whose horizontal location is the center of
203 the subsidence zone. Without dike opening, we could have only reproduced the
204 subsidence zone with smaller E-W extension displacement. The final position of the
205 dike segment was set where the RMS misfit was minimum. We thus estimated three
206 faults and one dike segment to explain the crustal deformation (Fig. 5). Our model is
207 similar to the geometry of Bear et al. (2008), regarding an east-dipping fault, two
208 west-dipping faults and a dike segment. After setting the location and geometry of the
209 fault sources and dike, we performed a linear least squares inversion to derive the
210 spatially variable slip and opening on the fault and dike, inverting jointly the ascending
211 and descending interferograms. Here we do not invert for the azimuth offset data, and
212 instead we check the consistency a posteriori as argued below. In solving the least
213 squares problem, we applied a “non-negativity” constraint. Namely, in order to derive
214 physically plausible slip distributions, we prescribed that the east-dipping and
215 west-dipping fault are allowed to slip right-laterally and left-laterally, respectively, and
216 that the dip slip on each segment has only normal slip component. The dike segment is
217 allowed to have only pure opening. Moreover, we apply a smoothing constraint on the

218 slip distribution by using an umbrella operator that is equivalent to the Laplacian
219 operator for the rectangular dislocation elements (Maerten et al. 2005). The moment
220 release from the fault slip distribution can be calculated, assuming Poisson ratio of 0.25
221 and shear modulus of 30 GPa.

222 The optimum fault slip and dike opening distribution on the each segment are shown
223 in Figs. 6. Each fault slip distribution has maximum amplitude around the depth of ~5
224 km with their amplitudes up to 60 cm in the strike slip and 160 cm in the dip slip. As
225 expected from the Global CMT solutions that indicate predominantly normal faulting,
226 the normal slip is much larger than the strike slip (Figs. 6b, d). However, the inferred
227 strike slip component is unexpectedly larger than that inferred by seismology (Figs. 6a,
228 c). The calculated geodetic moment for the dip slip component is 3.3×10^{18} Nm, and
229 that for the strike slip component is 8.1×10^{17} Nm. Thus, the contribution of the strike
230 slip is 19.9 %, and the equivalent moment magnitude for the dip slip and strike slip is
231 Mw 6.28 and 5.87, respectively. Because the cumulative seismic moment is 2.2×10^{18}
232 Nm according to the Global CMT, it turns out that about 56 % of the geodetic moment
233 were released aseismically. The moment for the strike slip must be responsible for the
234 southward movement of the subsidence zone. The dike segment exhibits up to 220 cm
235 opening at the depth of 2-4 km (Fig. 6g), and the volume of intrusion is 0.036 km^3 .

236 While we may include a Mogi-type deflation source to account for the source of the
237 intruded dike, we cannot identify any circular signals in the observed InSAR data that
238 allows us to constrain such a source. Although we do not discard the presence of a
239 deflation source, we consider that the depth of the Mogi source, if any, would be deeper
240 than 3 km, because otherwise there would arise circular fringes; we then assumed that
241 the Mogi source has the same volume changes as those of intruded dike. Moreover,
242 even if we include the deflation source at the center of the largest displacement field, the
243 E-W trending sharp offset at northern and southern edge of the negative signal will
244 never be generated.

245 Based on the inferred fault slip and dike opening distribution, we computed the ground
246 deformation (Figs. 2b, e) and misfit residual (Figs. 2c, f). RMS residual values in our
247 model are 3.0 cm in the ascending and 6.3 cm in the descending data. Although there
248 still remain some residuals in the eastern half of the descending data, the calculated
249 deformation well reproduces the observations, and the misfit residuals cannot be
250 distinguished from measurement errors that would be empirically less than 5 cm for a
251 single interferogram. Also, we calculated the displacements for the azimuth offset,
252 which also reproduces the characteristic offsets in the subsidence zone (Fig. 3).

253 Without the strike slip component, we could not reproduce the large azimuth offset

254 signals in the subsidence zone. Thus we conclude that the strike slip is necessary to
255 explain the observation results, and it occurred aseismically because almost all the
256 Global CMT solution exhibits the normal-dip slip.

257

258

259 **4. Discussion**

260 To our knowledge, not only the previous studies of the 2007 Lake Natron event, but
261 also many studies of dike intrusion events in rifts settings elsewhere assume normal slip
262 and dike opening in their fault source modeling (e.g., Wright et al.,2006; Nobile et al.,
263 2012; Baer and Hamiel, 2010; Hamling et al., 2014). Focal mechanisms of earthquakes
264 during the 2007 event indeed indicate few strike slip components. In contrast, the fault
265 source model we estimated in this study includes significant strike components, without
266 which we cannot reproduce the InSAR and azimuth offset observations. Considering the
267 few strike slip in the focal mechanisms, it turns out that aseismic strike components is
268 required to explain the ground deformation associated with the 2007 Natron event. Why
269 then did the aseismic strike slip occur at the area that is supposed to extend in the E-W
270 direction? Why did the subsiding area move toward the south that is orthogonal to the
271 rift axis?

272 In order to examine if the stress changes due to the dike intrusion promoted the fault
273 slips, we computed the Coulomb stress changes (ΔCFF), based on the our inferred fault
274 models (e.g., King et al., 1994; Toda et al., 2002). In the calculations of the ΔCFF , we
275 use a shear modulus of 30 GPa and a friction coefficient of 0.4. Fig. 7 illustrates the
276 distribution of the ΔCFF by the dike opening for each receiver fault at depths from the
277 surface to 6 km. We observe positive values of $\sim 0.05\text{MPa}$ at shallower depths,
278 suggesting unclamping, mainly distributed along the dike axis (Figs. 7a-f). In the
279 meantime, at the depths of 2-4 km at which we inferred the peak values of dike opening,
280 the negative ΔCFF (clamping) are widely distributed (Figs. 7j-r). Our inferred fault
281 models indicate significant slip distributions mostly at shallower depths, and thus are
282 mechanically consistent with the ΔCFF .

283 In the above ΔCFF modeling, however, we do not consider the background tectonic
284 stress fields. The two west-dipping faults are forming en-echelon structure, and the
285 strike components are much larger than the normal slip at the shallower depth of the
286 west-dipping fault to the northeastern end. There are many normal fault systems in the
287 EAR, which are forming relay zones and segmented structures (Ebinger, 1989;
288 Moustafa, 2002; Tesfaye et al., 2008). Relay zone is a geological structure formed by
289 multiple overlapping, en-echelon fault segments and develops under a transtensive

290 stress field instead of pure extension (Crider and Pollard, 1998).

291 The background stress field around the Lake Natron has been estimated from the focal
292 mechanisms of past earthquakes (Delvaux and Barth, 2010; The World Stress Map
293 available online at <http://www.world-stress-map.org>). Those studies indicate a pure
294 extension stress regime toward NNW-SSE around the Lake Natron. The NNW-SSE axis
295 is consistent with the orthogonal direction of the main shock strike direction during the
296 2007 event. Moreover, Delvaux and Barth (2010) and World Stress Map indicate
297 ENE-WSW pure extensive stress field in the Lake Manyara region, which is located 50
298 km to the south from the 2007 Natron rifting event area.

299 The stress field estimated from seismological studies, however, indicates
300 seismotectonic stresses, and the stress field can change at the other depths than the
301 depth of the employed hypocenters. It is likely that the existence of a microplate or
302 magma intrusion can build up a three-dimensionally complicated stress field. As shown
303 in the slip distribution in Fig. 6, the strike slip is dominating at the shallower depth,
304 suggesting the transcurrent stress regime. Meanwhile, it is well-known that the
305 shallowest zone of the crust exhibits a velocity-strengthening tendency in the friction
306 parameters of the rate-and-state dependent friction law, meaning the absence of seismic
307 slip and the presence of aseismic slip (Scholtz 1998). In other words, it should be noted

308 that we cannot infer a true stress regime at the shallowest depths from seismological
309 studies, no matter what type of stress fields are dominant. Thus we may claim that this
310 study is the first to have confirmed the transtensive stress regime at shallower depth
311 around the Lake Natron by the detection of the aseismic strike slip based on the InSAR
312 data. Although Wright et al. (2006) suggested that dike intrusion is essential to form the
313 along-axis segmentation, and we do not dispute its importance, our detection of
314 significant strike slip at shallow depth is a direct evidence for the presence of
315 transtensive stress that is necessary to generate the along-axis segmentation like relay
316 zone (transfer zone). We consider that the dike intrusion could contribute to generate the
317 three-dimensionally complex stress distributions. Since our dike opening model sets a
318 kinematic displacement boundary condition instead of stress boundary condition, we
319 should note that the stress axis around the study area does not have to coincide with the
320 dike opening direction.

321 The relay ramp is known to form between antithetic normal faults like graben structure
322 (Tesfaye et al., 2008; Amer et al., 2012). As the relay ramp develops, a fracture can be
323 built up along the direction orthogonal to the fault strike direction, generating new
324 normal faults as transfer faults (Xu et al., 2011; Commins et al., 2005). Such fractures
325 are also observed at the Northern Lake Rukwa (Chorowitz, 2005). While we do not

326 include it in the source model of this study, we can identify such discontinuities in the
327 azimuth offset observation as indicated by the red dashed line (Fig. 3). We consider that
328 those discontinuities would also be the evidence for the horizontal motion of the
329 subsiding region.

330 The observed aseismic slip may also have an important implication for the generation
331 mechanism of earthquake swarms (e.g., Lohman and McGuire, 2007; Takada and
332 Furuya, 2010; Wicks et al., 2011). Earthquake swarms are often attributed to fluid or
333 magma intrusion, and it is apparent that such an intrusion occurred during our recording
334 period. However, besides the dike intrusion process, aseismic slip has also been
335 proposed as another possible driver of swarm generation. We may regard the detected
336 aseismic strike slip as another piece of evidence for the proposed swarm mechanism.

337

338 **5. Conclusion**

339 Using ALOS/PALSAR data, we have detected the ground displacements associated
340 with the 2007 northern Tanzanian earthquake swarm episode near the Lake Natron. In
341 addition to the two-pass InSAR data from both ascending and descending paths, we
342 derived azimuth offset data that are sensitive to the displacements parallel to the satellite
343 flight direction. We could thus demonstrate the 3D displacement fields. Besides the

344 graben-like structure already pointed out in the previous studies, the 3D displacement
345 fields indicate that the subsidence zone moved toward SSW.

346 Our fault source model consists of one tensile-opening fault, one east-dipping fault,
347 and two west-dipping faults. One notable difference of our fault model from previous
348 studies is the presence of strike slip component that turns out to contribute to
349 approximately 20 % of the whole moment release. Because the focal mechanisms of the
350 earthquakes during the 2007 swarm event represent nearly pure normal faulting, we
351 consider that aseismic strike slip on the faults are responsible for the horizontal
352 movement of the subsidence zone.

353

354

355 *Acknowledgement*

356 We generated all of the interferograms and pixel-offset data from Phased Array-Type
357 L-Band Synthetic Aperture Radar (PALSAR) level 1.0 data, using the commercial
358 software package from GAMMA Remote Sensing. PALSAR level 1.0 data used in this
359 study are shared among the PALSAR Interferometry Consortium to Study our Evolving
360 Land surface (PIXEL) , and provided from JAXA under a cooperative research contract
361 with the Earthquake Research Institute, University of Tokyo. The ownership of

362 PALSAR data belongs to JAXA and the Ministry of Economy, Trade and Industry
363 (METI). The Global Centroid Moment Tensor Project database was searched using
364 www.globalcmt.org/CMTsearch.html (last accessed July 2014). Some of the figures in
365 this paper were made by Matlab (<http://www.mathworks.com>, last accessed January
366 2015). Some figures were prepared using the public domain Generic Mapping Tools
367 (GMT). We thank the anonymous reviewer and the Editor for their careful reading and
368 comments, which we believe were helpful to improve the original manuscript.

369

370

371 *Reference*

372 Albaric, J., Perrot, J., Déverchère, J., Deschamps, A., Le Gall, B., Ferdinand, R.W., Petit,
373 C., Tiberi, C., Sue, C., Songo, M., 2010. Contrasted seismogenic and rheological
374 behaviours from shallow and deep earthquake sequences in the North Tanzanian
375 Divergence, East Africa. *J. African Earth Sci.* 58, 799–811.
376 doi:10.1016/j.jafrearsci.2009.09.005

377

378 Amer, R., Mohamed, S., Robert, R., John, E., 2012. Structural architecture for
379 development of marginal extensional sub-basins in the Red Sea Active Rift Zone. *Int. J.*
380 *Geosci.* 2012, 133–152.

381

382 Aoki, Y., 1999. Imaging Magma Transport During the 1997 Seismic Swarm off the Izu

383 Peninsula, Japan. *Science*. 286, 927–930. doi:10.1126/science.286.5441.927
384

385 Baer, G., Hamiel, Y., Shamir, G., Nof, R., 2008. Evolution of a magma-driven
386 earthquake swarm and triggering of the nearby Oldoinyo Lengai eruption, as resolved
387 by InSAR, ground observations and elastic modeling, East African Rift, 2007. *Earth*
388 *Planet. Sci. Lett.* 272, 339–352. doi:10.1016/j.epsl.2008.04.052
389

390 Baer, G., Hamiel, Y., 2010. Form and growth of an embryonic continental rift: InSAR
391 observations and modelling of the 2009 western Arabia rifting episode. *Geophys. J. Int.*
392 182, 155–167. doi:10.1111/j.1365-246X.2010.04627.x
393

394 Bechor, N.B.D., Zebker, H.A., 2006. Measuring two-dimensional movements using a
395 single InSAR pair. *Geophys. Res. Lett.* 33, L16311.
396

397 Biggs, J., Amelung, F., Gourmelen, N., Dixon, T.H., Kim, S., 2009. InSAR observations
398 of 2007 Tanzania rifting episode reveal mixed fault and dyke extension in an immature
399 continental rift. *Geophys. J. Int.* 179, 549–558. doi:10.1111/j.1365-246X.2009.04262.x
400

401 Calais, E., D’Oreye, N., Albaric, J., Deschamps, A., Delvaux, D., Déverchère, J.,
402 Ebinger, C., Ferdinand, R.W., Kervyn, F., Macheyeke, A.S., Oyen, A., Perrot, J., Saria,
403 E., Smets, B., Stamps, D.S., Wauthier, C., 2008. Strain accommodation by slow slip and
404 dyking in a youthful continental rift, East Africa. *Nature* 456, 783–788.
405

406 Chorowicz, J., 2005. The East African rift system. *J. African Earth Sci.* 43, 379–410.

407 doi:10.1016/j.jafrearsci.2005.07.019

408

409 Commins, D., Gupta, S., Cartwright, J., 2005. Deformed streams reveal growth and
410 linkage of a normal fault array in the Canyonlands graben, Utah. *Geol. Soc. Am.* 33,
411 645–648. doi:10.1130/G21433.1

412

413 Crider, J.G., Pollard, D.D., 1998. Fault linkage: Three-dimensional mechanical
414 interaction between echelon normal faults. *J. Geophys. Res.* 103, 24373.
415 doi:10.1029/98JB01353

416

417 Delvaux, D., Barth, A., 2010. African stress pattern from formal inversion of focal
418 mechanism data. *Tectonophysics* 482, 105–128. doi:10.1016/j.tecto.2009.05.009

419

420 Dawson, JB, JV Smith, and IM Steele. 1992. “1966 Ash Eruption of the Carbonatite
421 Volcano Oldoinyo Lengai: Mineralogy of Lapilli and Mixing of Silicate and Carbonate
422 Magmas.” *Mineralogical Magazine* 56, 382, 1–16.

423

424 Ebinger, C., 1989. Tectonic development of the western branch of the East African rift
425 system. *Geol. Soc. Am. Bull.* doi:10.1130/0016-7606(1989)101<0885

426

427 Farr, T.G., Rosen, P., Caro, E., Crippen, R., 2007. The shuttle radar topography mission.
428 *Rev. Geophys.* 45, 1–33. doi:10.1029/2005RG000183

429

430 Fialko, Y., Simons, M., Agnew, D., 2001. The complete (3-D) surface displacement field

431 in the epicentral area of the 199 Mw7.1 Hector Mine earthquake, California, from space
432 geodetic observation. *Geophys. Res. Lett.* 28, 3063–3066.

433

434 Fukushima, Y., Cayol, V., Durand, P., Massonnet, D., 2010. Evolution of magma
435 conduits during the 1998–2000 eruptions of Piton de la Fournaise volcano, Réunion
436 Island. *J. Geophys. Res.* 115, B10204. doi:10.1029/2009JB007023

437

438 Furuya, M., Yasuda, T., 2011. The 2008 Yutian normal faulting earthquake (Mw 7.1),
439 NW Tibet: Non-planar fault modeling and implications for the Karakax Fault.
440 *Tectonophysics* 511, 125–133. doi:10.1016/j.tecto.2011.09.003

441

442 Geuzaine, C., Remacle, J.-F., 2009. Gmsh: A 3-D finite element mesh generator with
443 built-in pre- and post-processing facilities. *Int. J. Numer. Methods Eng.* 79, 1309–1331.
444 doi:10.1002/nme.2579

445

446 Global CMT project at <http://www.globalcmt.org> [Last accessed October 2014]

447

448 Goldstein, R.M., Zebker, H. a., Werner, C.L., 1988. Satellite radar interferometry:
449 Two-dimensional phase unwrapping. *Radio Sci.* 23, 713–720.
450 doi:10.1029/RS023i004p00713

451

452 Hamling, I.J., Ayele, A., Bennati, L., Calais, E., Ebinger, C.J., Keir, D., Lewi, E., Wright,
453 T.J., Yirgu, G., 2009. Geodetic observations of the ongoing Dabbahu rifting episode:
454 new dyke intrusions in 2006 and 2007. *Geophys. J. Int.* 178, 989–1003.

455 doi:10.1111/j.1365-246X.2009.04163.x

456

457 Hamling, I.J., Wright, T.J., Calais, E., Lewi, E., Fukahata, Y., 2014. InSAR observations
458 of post-rifting deformation around the Dabbahu rift segment, Afar, Ethiopia. *Geophys. J.*
459 *Int.* 1–17.

460

461 Hanssen, R.F., Feijt, A.J., Klees, R., 2001. Comparison of Precipitable Water Vapor
462 Observations by Spaceborne Radar Interferometry and Meteosat 6.7- μ m Radiometry 18,
463 756–764.

464

465 Jonsson, S., Zebker, H., Segall, P., Amelung, F., 2002. Fault Slip Distribution of the
466 1999 Mw7.1 Hector Mine, California, Earthquake, Estimated from Satellite Radar and
467 GPS Measurements. *Bull. Seismol. Soc. Am.* 92, 1377–1389.

468

469 King, G.C.P., Stein, S., Lin, J., 1994. Static Stress Changes and the Triggering of
470 Earthquakes. *Bull. Seismol. Soc. Am.* 84, 935–953.

471

472 Lohman, R.B., McGuire, J.J., 2007. Earthquake swarms driven by aseismic creep in the
473 Salton Trough, California. *J. Geophys. Res.* 112, B04405. doi:10.1029/2006JB004596

474

475 Maerten, F., 2005. Inverting for Slip on Three-Dimensional Fault Surfaces Using
476 Angular Dislocations. *Bull. Seismol. Soc. Am.* 95, 1654–1665.

477 doi:10.1785/0120030181

478

479 Massonnet, D., Feigl, K.L., 1998. Radar interferometry and its application to changes in
480 the Earth's surface. *Rev. Geophys.* 36, 441–500.
481

482 Mattsson, Hannes B., and Barbara a. Tripoli. 2011. “Depositional Characteristics and
483 Volcanic Landforms in the Lake Natron–Engaruka Monogenetic Field, Northern
484 Tanzania.” *Journal of Volcanology and Geothermal Research* 203, 23–34.
485 doi:10.1016/j.jvolgeores.2011.04.010.
486

487 McKenzie, D., Davies, D., Molnar, P., 1970. Plate tectonics of the Red Sea and East
488 Africa. *Nature* 226, 243–248.
489

490 Meade, B.J., 2007. Algorithms for the calculation of exact displacements, strains, and
491 stresses for triangular dislocation elements in a uniform elastic half space. *Comput.*
492 *Geosci.* 33, 1064–1075. doi:10.1016/j.cageo.2006.12.003
493

494 Moustafa, A., 2002. Controls on the geometry of transfer zones in the Suez rift and
495 northwest Red Sea: Implications for the structural geometry of rift systems. *Am. Assoc.*
496 *Pet. Geol. Bull.* 6, 979–1002.
497

498 Nobile, A., Pagli, C., Keir, D., Wright, T.J., Ayele, A., Ruch, J., Acocella, V., 2012.
499 Dike-fault interaction during the 2004 Dallol intrusion at the northern edge of the Erta
500 Ale Ridge (Afar, Ethiopia). *Geophys. Res. Lett.* 39. doi:10.1029/2012GL053152
501

502 Okada, Y., 1985. Surface deformation due to shear and tensile faults in a half-space.

503 Bull. Seismol. Soc. Am. 75, 1135–1154.
504
505 Paquet, F., Dauteuil, O., Hallot, E., Moreau, F., 2007. Tectonics and magma dynamics
506 coupling in a dyke swarm of Iceland. *J. Struct. Geol.* 29, 1477–1493.
507 doi:10.1016/j.jsg.2007.06.001
508
509 Saria, E., Calais, E., 2014. Present - day kinematics of the East African Rift. *J. Geophys.*
510 *Res. Solid Earth* 3584–3600. doi:10.1002/2013JB010901
511
512 Scholz, C., Contreras, J., 1998. Mechanics of continental rift architecture. *Geology* 26,
513 967–970.
514
515 Stamps, D.S., Calais, E., Saria, E., Hartnady, C., Nocquet, J.-M., Ebinger, C.J.,
516 Fernandes, R.M., 2008. A kinematic model for the East African Rift. *Geophys. Res. Lett.*
517 35, L05304. doi:10.1029/2007GL032781
518
519 Takada, Y., Furuya, M., 2010. Aseismic slip during the 1996 earthquake swarm in and
520 around the Onikobe geothermal area, NE Japan. *Earth Planet. Sci. Lett.* 290, 302–310.
521 doi:10.1016/j.epsl.2009.12.024
522
523 Tesfaye, S., Rowan, M.G., Mueller, K., Trudgill, B.D., Harding, D.J., 2008. Relay and
524 accommodation zones in the Dobe and Hanle grabens, central Afar, Ethiopia and
525 Djibouti. *J. Geol. Soc. London.* 165, 535–547. doi:10.1144/0016-76492007-093
526

527 Toda, S., Stein, R.S., Sagiya, T., 2002. Evidence from the AD 2000 Izu islands
528 earthquake swarm that stressing rate governs seismicity. *Nature* 419, 58–61.
529 doi:10.1038/nature00997

530

531 Wegmüller, U., and C. L. Werner (1997). Gamma SAR processor and interferometry
532 software, in *Proc. of the 3rd ERS Symposium*, EuropeanSpace Agency Special
533 Publication, ESA SP-414, Florence, Italy, 14–21 March 1997, 1686–1692.

534

535 Wicks, C., Thelen, W., Weaver, C., Gomberg, J., Rohay, A., Bodin, P., 2011. InSAR
536 observations of aseismic slip associated with an earthquake swarm in the Columbia
537 River flood basalts. *J. Geophys. Res.* 116. doi:10.1029/2011JB008433

538

539 World Stress Map at <http://www.world-stress-map.org> [Last accessed November 2014]

540

541 Wright, T.J., Ebinger, C., Biggs, J., Ayele, A., Yirgu, G., Keir, D., Stork, A., 2006.
542 Magma-maintained rift segmentation at continental rupture in the 2005 Afar dyking
543 episode. *Nature* 442, 291–294. doi:10.1038/nature04978

544

545 Xu, S., Ángel Francisco, N.-S., Susana, A.A.-Á., Luis, M.C.-M., 2011. Structural
546 analysis of a relay ramp in the Querétaro graben, central Mexico: Implications for relay
547 ramp development. *Rev. Mex.* 28, 275–289.

548

549

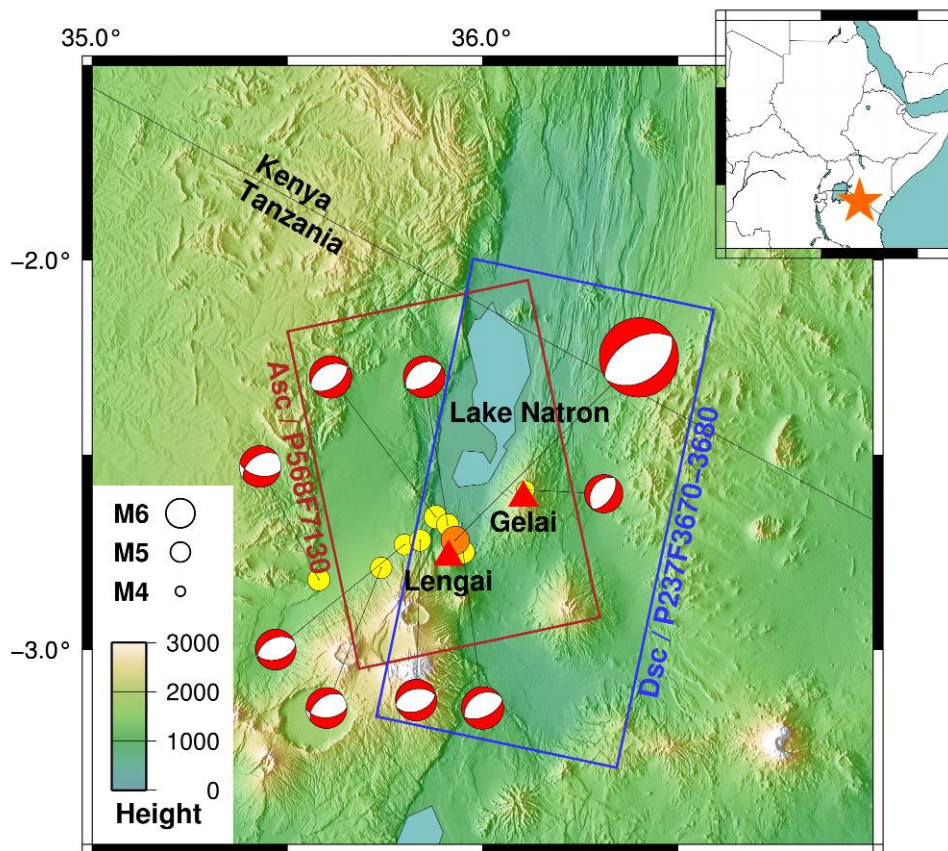
550

551 **Table 1**

552 The ALOS/PALSAR data sets in this study

Pair No.	Data(yyyy/mm/dd)	Orbit	Path	Frame	Bperp [m]
1	20070707-20071007	Ascending	568	7130	-249.05
2	20070605-20100613	Descending	237	3670-3680	-396.21

553

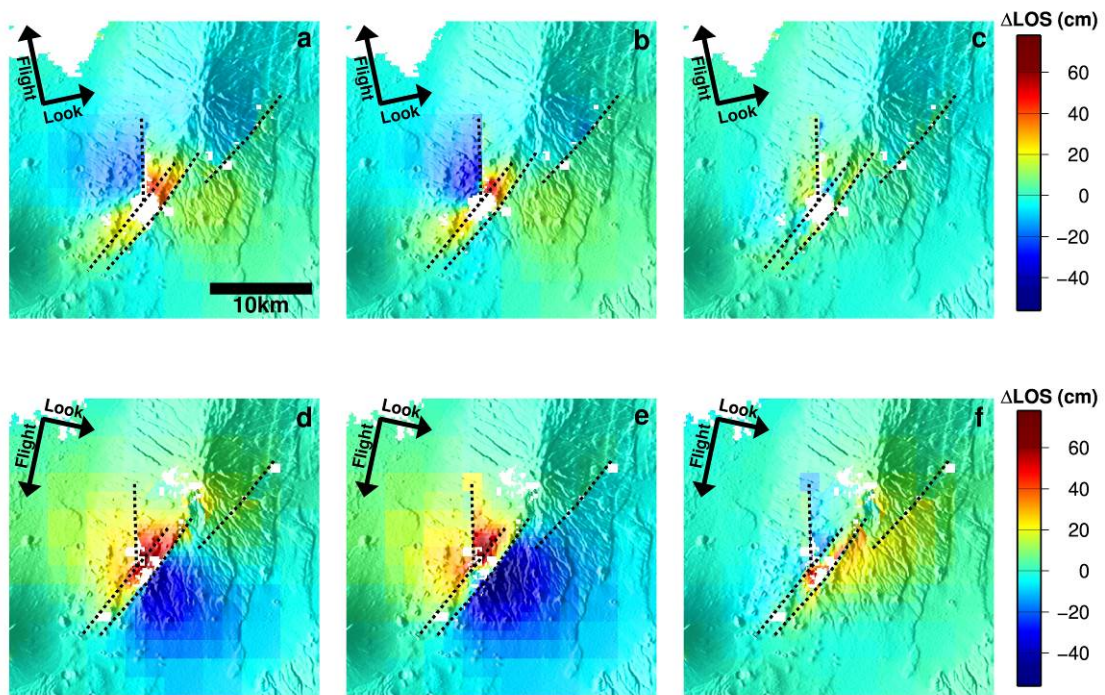


554

555 **Fig. 1.** Our study area is located to the south of Lake Natron, Northern Tanzania, near
556 the Kenyan border (upper-right map). Yellow circles and beach balls show the
557 earthquake epicenters and focal mechanisms, respectively, during the 2007 episode
558 ($M > 5$, source Global CMT catalogue), and the largest beach ball indicates the main

559 shock of focal mechanism (M5.9). Red and blue rectangles mark the imaged area by
 560 ALOS/PALSAR (c.f. Table 1).

561



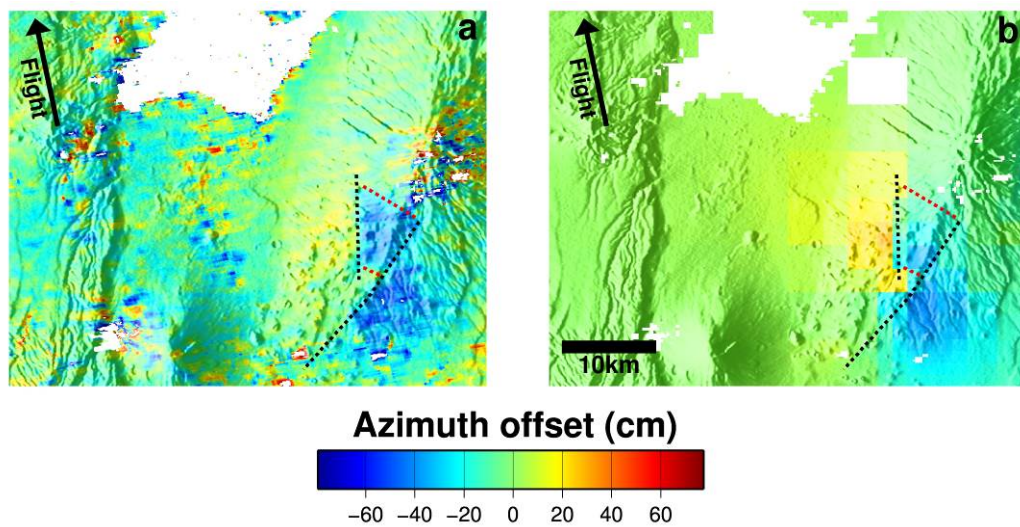
562

563 **Fig. 2.** (a, d) Observed unwrapped interferograms covering the 2007 event derived from
 564 (a) ascending and (b) descending track. (b, e) Calculated interferograms from the
 565 inferred fault slip distribution in Fig. 6 for (b) ascending and (e) descending. (c, f) Misfit
 566 residuals between the observed and calculated for (c) ascending and (f) descending. The
 567 unit vector of line of sight is $(e_e, e_n, e_z) = (0.613, 0.131, -0.779)$ for ascending and $(e_e,$
 568 $e_n, e_z) = (-0.612, 0.131, -0.780)$ for descending, respectively. Black dot lines indicate the

569 top of the faults. Two arrows in each figure indicate the satellite flight direction and
570 beam radiation direction.

571

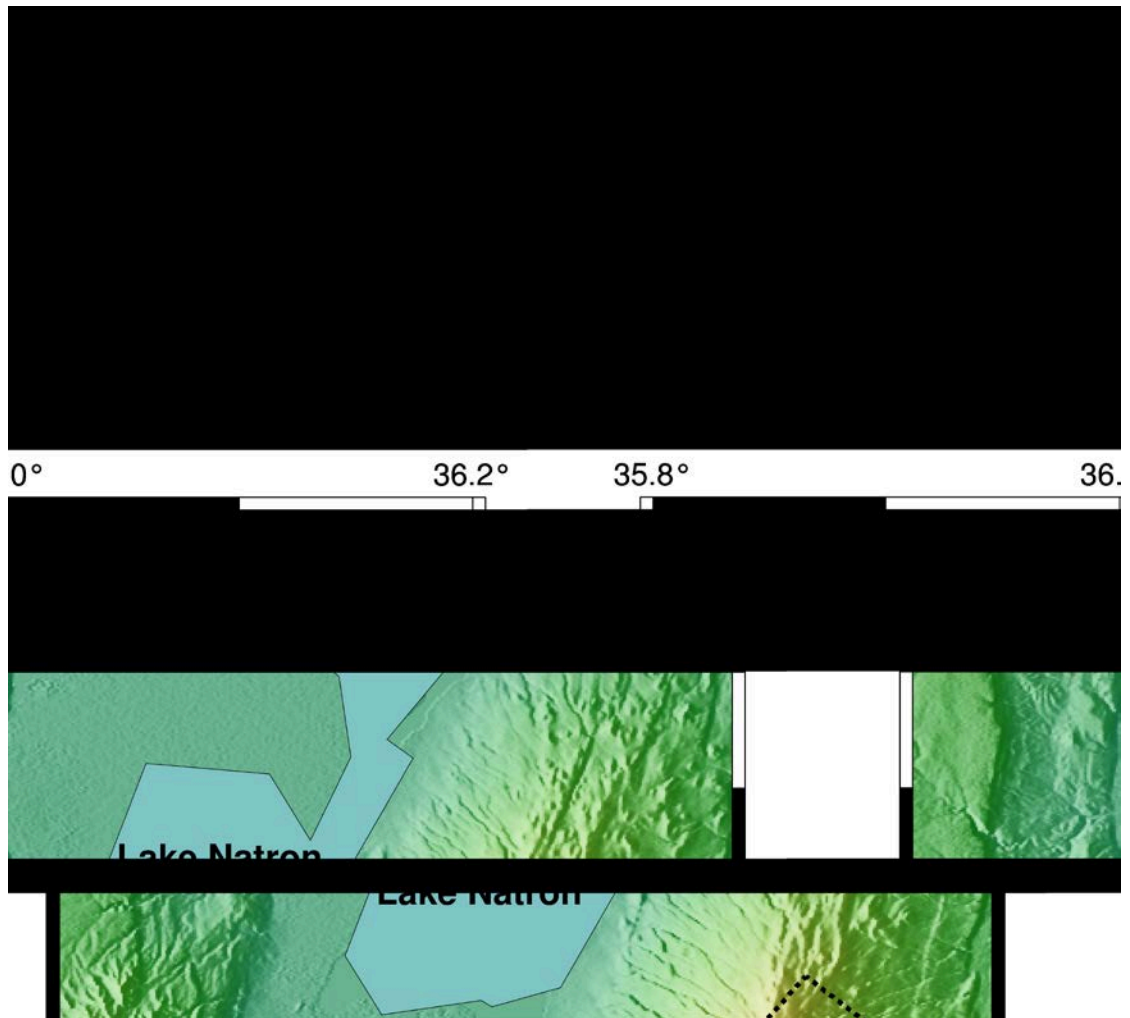
572



573

574 **Fig. 3.** (a) Observed azimuth offset derived from the ascending pair. (b) Calculated
575 azimuth offset from the estimated slip distributions in the estimated from fault source
576 modeling. Black dashed lines mark the top of the two facing faults. The two phase
577 discontinuities along the direction orthogonal to the fault strike as indicated by the red
578 dashed lines. The arrow in the top left indicates the flight direction of the satellite, and
579 the unit vector is $(e_e, e_n, e_z) = (-0.209, 0.978, 0)$.

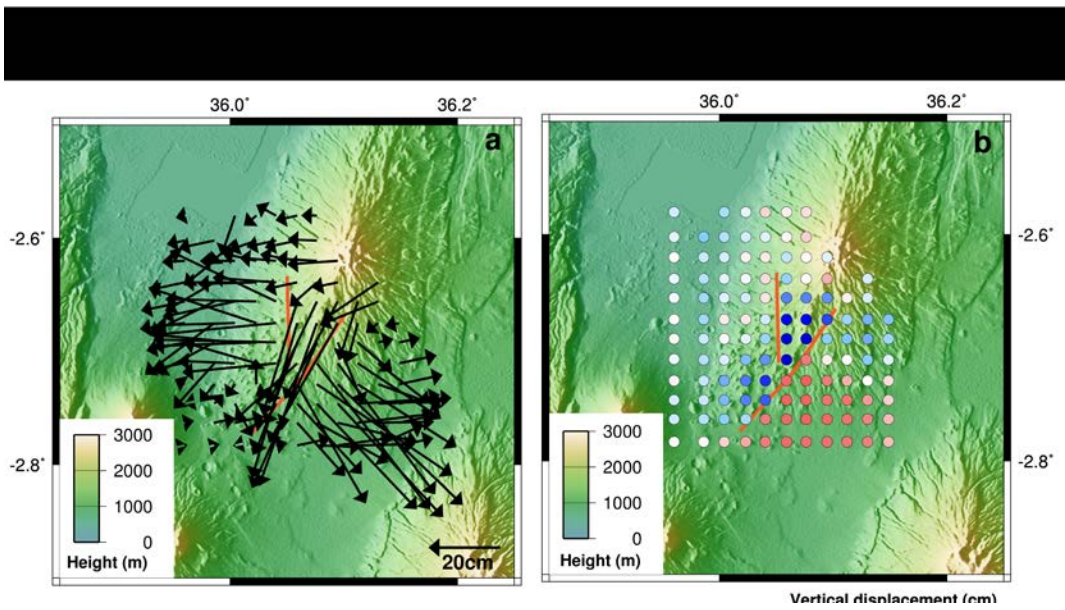
580



581

582 **Fig. 4.** Surface projection and 3D display of the fault model geometry. (Left) Solid lines
 583 mark the top edge of the faults, and the dashed lines indicate the side and bottom edges
 584 of the faults. Red indicates the location of the dike segment. (Right) Blue segments
 585 indicate east-dipping faults, green segment is east-dipping fault, and red segment is dike.
 586 The inferred slip distributions are shown in Figs. 6.

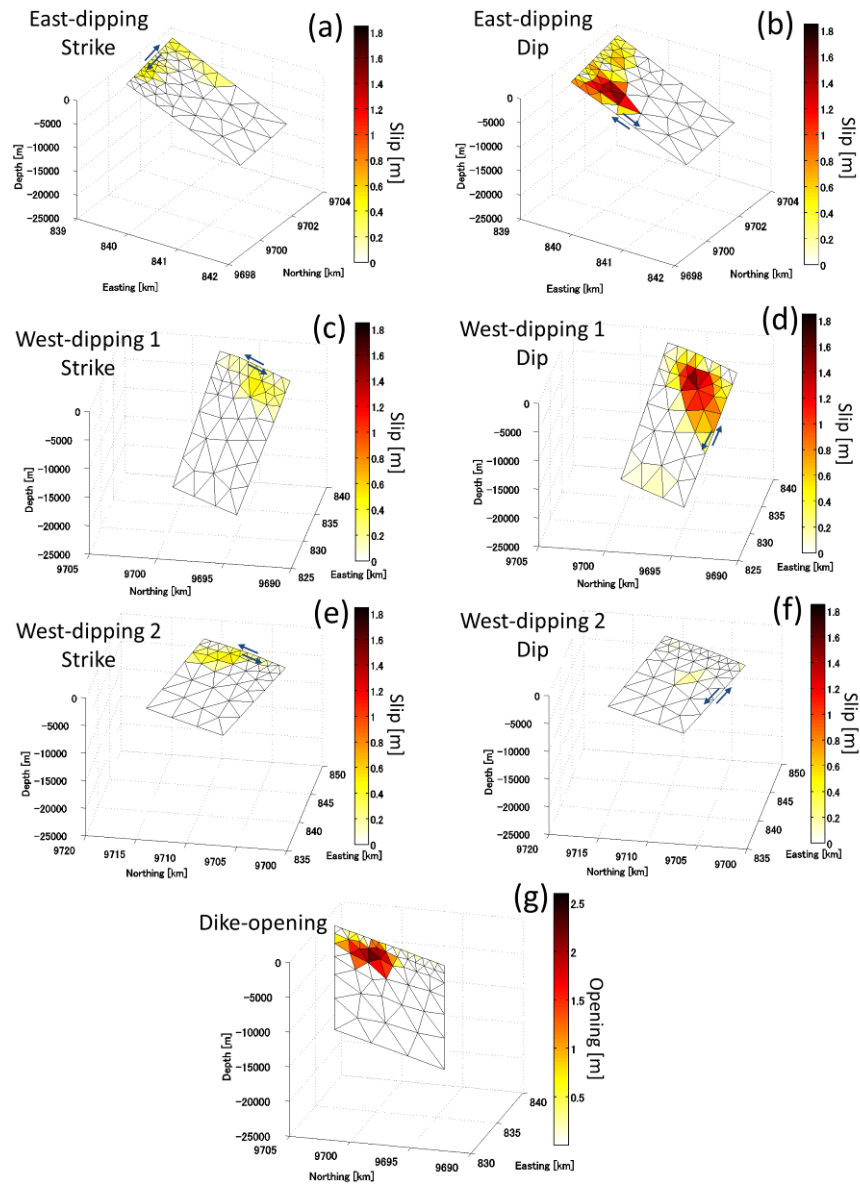
587



588

589 **Fig. 5.** Inferred 3D displacement using both ascending, descending interferograms and
 590 the azimuth offset tracking in the azimuth direction. (a) Horizontal displacements. (b)
 591 Vertical displacements. Orange lines in each figure follow the top of the confronted
 592 faults.

593



594

595 **Fig. 6.** Estimated slip distribution for each segments. See the texts for details. (a, b) Slip

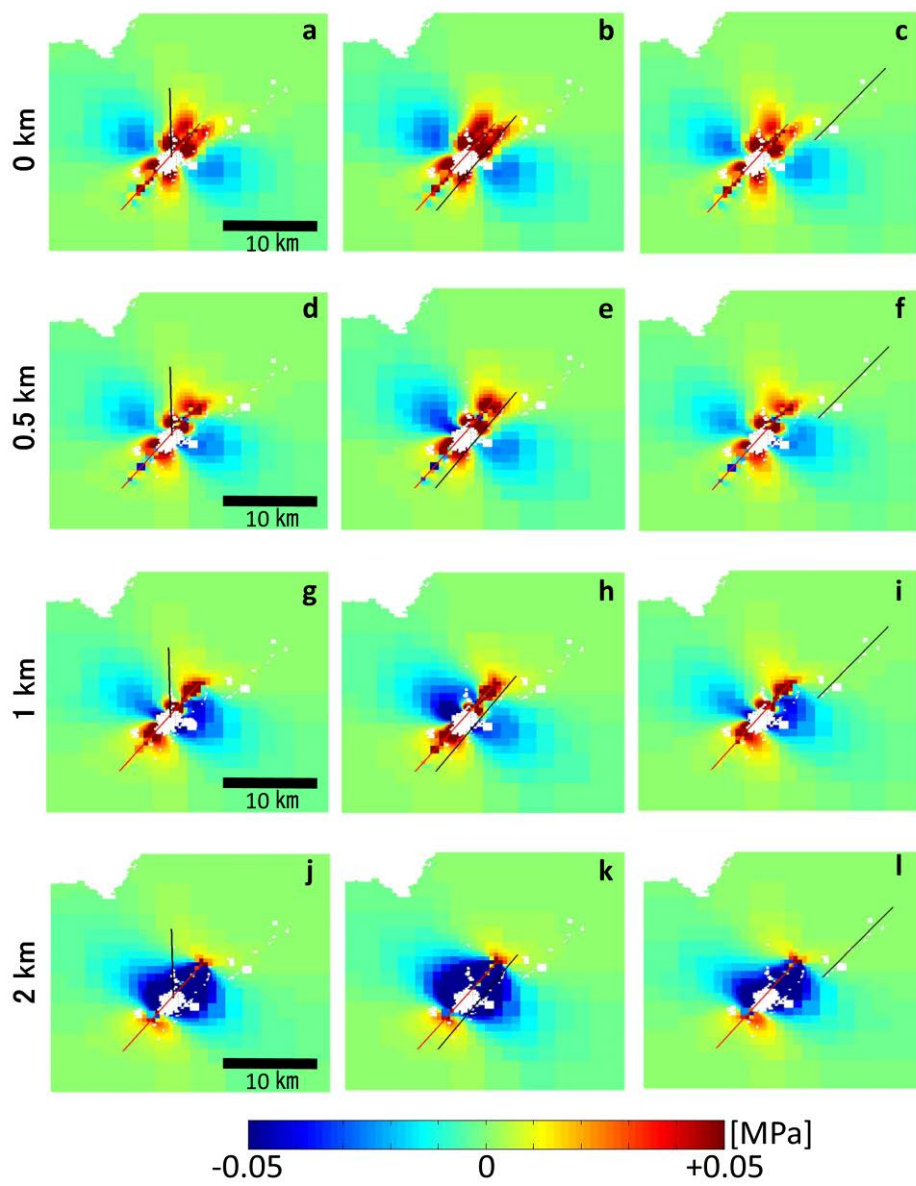
596 distributions were shown on the east-dipping fault. (c, d) West-dipping fault 1 is one of

597 the confronted faults. (e, f) West-dipping fault 2 located at the eastern flank of Mt. Gelai.

598 Slip direction are shown as vector in the figures. (g) Dike was imposed pure opening.

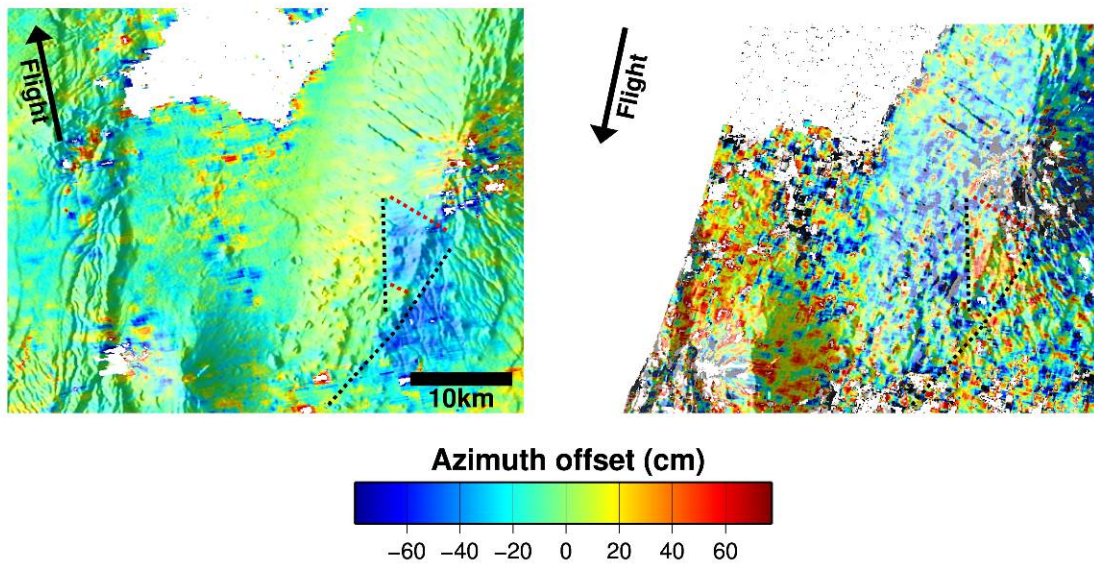
599 The arrows indicate slip directions of each the faults. The unit of dislocation or

600 opening is indicated with meter scale. The rake angle for each angles are -77.6, -100.1,
 601 -167.6 degrees measures clockwise from the north in the east-dipping, west-dipping 1,
 602 west-dipping 2 fault, respectively.
 603

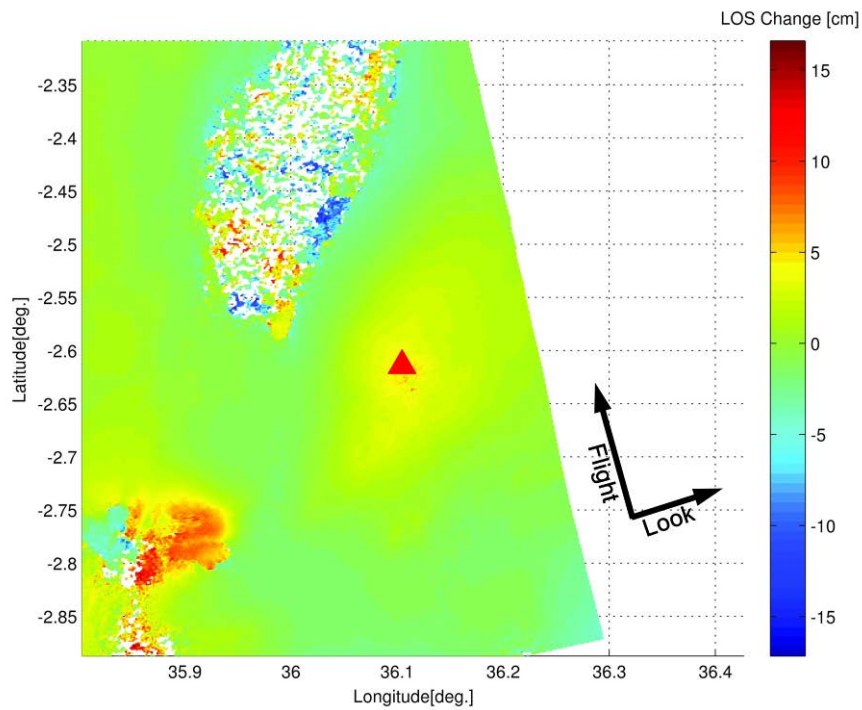


604
 605 **Fig. 7.** Coulomb stress changes for the receiver faults (black lines) due to the dike

606 opening as the source fault (red line). The top edges of the receiver faults are shown as
 607 black lines (Left column: East-dipping fault, Center: West-dipping fault, Right: Shallow
 608 west-dipping fault). Stress changes indicate positive (unclamping) the near surface, and
 609 the most negative (clamping) at the depth of maximum dike opening around 2-3 km.
 610



611
 612 **Fig. S1.** The observed azimuth offset derived from the ascending (left) and descending
 613 data (right) respectively; the left one is the same as Fig 3a. Arrows show the satellite
 614 flight directions, and the azimuth offsets are sensitive to such displacements that are
 615 parallel to the flight direction. Incoherent area is masked. Black dots lines indicate the
 616 top location of the confronted faults (see section 3).
 617



618

619 **Fig. S2.** The post-rifting ascending interferogram spanning 7 Oct. 2007 - 15 Jul. 2010.

620 Red triangle indicates the location of Mt. Gelai and top-left noisy area is Lake Natron

621 and bottom-left signal shows deformation associated with the eruption of Mt. Oldoinyo

622 Lengai.